Remote Sensing of Environment 186 (2016) 358–371

Contents lists available at ScienceDirect

Remote Sensing of Environment

journal homepage: www.elsevier.com/locate/rse

Variations in ice velocities of Pine Island Glacier Ice Shelf evaluated using multispectral image matching of Landsat time series data

Hyangsun Han [a,b], Jungho Im [a,*], Hyun-cheol Kim [b]

[a] School of Urban and Environmental Engineering, Ulsan National Institute of Science and Technology, Ulsan, South Korea
[b] Division of Polar Ocean Environment, Korea Polar Research Institute, Incheon, South Korea

ARTICLE INFO

Article history:
Received 5 June 2015
Received in revised form 10 August 2016
Accepted 5 September 2016
Available online 10 September 2016

Keywords:
Pine Island Glacier Ice Shelf
Ice velocity
Strain rate
Landsat
Multispectral image matching

ABSTRACT

Pine Island Glacier (PIG) in West Antarctica drains out to the Amundsen Sea through Pine Island Glacier Ice Shelf (PIGIS). As changes in ice velocities on PIGIS are strongly linked to changes in ice mass discharge from the West Antarctic Ice Sheet, it is very important to evaluate the spatiotemporal variations in ice velocities on the ice shelf. This research estimated ice velocities of PIGIS from an ensemble of image matching of Landsat time series multispectral data obtained from 2000 to 2014. Orientation correlation was adopted for the image matching of blue, green, red, near infrared, panchromatic, and the first principal image of the Landsat multispectral data, from which the results were combined and averaged. The multispectral image matching proposed in this research produced ~35% more ice velocity vectors than the use of a single band (i.e., panchromatic band) image matching. The erroneous matches were filtered through simple but rigorous statistical evaluations. The ice velocity of PIGIS accelerated by ~55% during 2000–2010, and the acceleration of the image northing velocity component (~1.3 km a^{-1}) was higher than that of the image easting velocity component (~0.8 km a^{-1}). During 2010–2012, the ice velocity of PIGIS slowed down by ~10%. The ice velocity in 2014 increased by 5% from 2012, but was still lower than the peak values observed in 2010. The surface strain rate fields of PIGIS were derived from the ice velocity fields. The longitudinal ice compression was observed near the grounding line and the geographically northern part of the central ice shelf of PIGIS, while a fast-flowing band was observed near the southern margin of the ice shelf. The transverse strain rate showed that ice divergence in the hinge zone of the central ice shelf has increased since 2000. The width of the shear margins of the central ice shelf of PIGIS is ~25 km, which has been stable since 2000.

1. Introduction

Ice shelves are permanent floating platforms of ice that extend from grounded glaciers or ice streams. In Antarctica, ice shelves are attached to ~75% of the Antarctic coastline and their total extent is reported as ~1.56 million km^2 during 2003–2008 (Rignot et al., 2013). They buttress the movement of the Antarctic Ice Sheet flowing into the ocean (Dupont and Alley, 2005). The velocity variations of ice shelves can affect changes in thickness, area, and iceberg calving rate of the ice shelves, which could make unstable buttressing of the ice sheet by the ice shelves and affect the distribution of landfast sea ice (De Angelis and Skvarca, 2003; Rignot et al., 2004; Scambos et al., 2004; Dupont and Alley, 2005; Khazendar et al., 2011; Kim et al., 2015b). The velocity variations of ice shelves in West Antarctica, especially in the Amundsen Sea Embayment are more dramatic than that in East Antarctica (Mouginot et al., 2014). Ice velocities of Pine Island Glacier Ice Shelf, Thwaites Ice Tongue and Crosson Ice Shelf, representative ice shelves in the Amundsen Sea Embayment have sped up by ~70% from the 1970s to 2013, showing an increase in ice discharge at grounding lines from 189 Gt a^{-1} to 334 Gt a^{-1} (Mouginot et al., 2014).

Pine Island Glacier (PIG), one of the largest ice streams in West Antarctica, flows into Pine Island Bay in the Amundsen Sea and feeds a floating ice mass, i.e. the Pine Island Glacier Ice Shelf (PIGIS). The ice flux discharge at the grounding line of PIG increased by ~50 Gt a^{-1} in the last 40 years, contributing to ~40% of the total ice flux in the Amundsen Sea (Mouginot et al., 2014), which is specifically attributed to fast acceleration of PIG. Between 1973 and 2010, PIGIS accelerated by 75% which is the highest acceleration in the Amundsen Sea Embayment (Mouginot et al., 2014). The velocity variations of PIGIS can give information about the changing conditions of climate drivers acting on the ice shelf such as ocean-induced basal melting, thinning and reduced buttressing stress (Rignot et al., 2002; Bindschadler et al., 2011). Therefore, it is crucial to evaluate the variations in ice velocity of PIGIS to monitor environmental changes in West Antarctica and to better understand global climate change.

The ice velocity of glaciers can be measured by Interferometric Synthetic Aperture Radar (InSAR) and image matching of the repeatedly

* Corresponding author.
E-mail address: ersgis@unist.ac.kr (J. Im).

http://dx.doi.org/10.1016/j.rse.2016.09.001
0034-4257/

obtained SAR or optical data. InSAR has been widely used to measure ice velocity (Forster et al., 2003; Rignot et al., 2002; Joughin, 2002; Young and Hyland, 2002; Rignot et al., 2011a; Han and Lee, 2015). For fast-flowing ice such as PIGIS, only InSAR pairs with a very short temporal baseline, such as one-day, are suitable to measure ice velocity due to temporal decorrelation of the ice surface (Han and Lee, 2015). However, the acquisition of such InSAR pairs is very difficult and expensive. Even if it is possible to obtain InSAR pairs with a short temporal baseline, it is still difficult to measure the velocity of an ice shelf. This is because InSAR signals of an ice shelf include both the gravitational ice flow in the horizontal direction and the tidal-induced deflection in the vertical direction (Rignot et al., 2011b; Han and Lee, 2014; Han and Lee, 2015). To measure the ice velocity of an ice shelf by InSAR, several studies removed the vertical tidal deflection of ice shelves from InSAR signals by using tide heights predicted by tide models (Wen et al., 2010; Scheuchl et al., 2012). However, they could not measure accurate ice velocity in hinge zones where a hydrostatic equilibrium assumption is not valid. While Han and Lee (2015) proposed a method to estimate ice velocity in a hinge zone using a double-differential InSAR (DDInSAR) technique, their method requires the continuous acquisitions of InSAR pairs with very short temporal baselines.

An image matching technique finds the displacement of features by calculating the optimal correlation between two images obtained sequentially over a region, which can be used to measure the ice velocity of fast-flowing glaciers. Various image matching methods have been developed and applied to SAR and optical image pairs to measure ice velocities (Scambos et al., 1992; Strozzi et al., 2002; Kääb, 2005; Haug et al., 2010; Ahn and Howat, 2011; Debella-Gilo and Kaab, 2011; Debella-Gilo and Kaab, 2012; Heid and Kaab, 2012; Warner and Roberts, 2013; Kim et al., 2015a). Image matching of SAR data can be very useful for the measurement of Antarctic ice velocities because it can produce correct matches regardless of sun altitudes and weather conditions. However, ground coverage of most SAR images is typically less than ~100 km^2 and thus many images are required to cover a large glacier or ice shelf. On the other hand, optical sensors of medium to low spatial resolution (15 m–1 km) such as Landsat-8 Operational Land Imager (OLI) (15–30 m resolution), Landsat-7 Enhanced Thematic Mapper Plus (EMT+) (15–60 m resolution), Landsat-5 Thematic Mapper (TM) (15–120 m resolution), Terra Advanced Spaceborne Thermal Emission and Reflectance Radiometer (ASTER) (15–90 m resolution), and Terra/Aqua Moderate Resolution Imaging Spectroradiometer (MODIS) (250 m–1 km resolution) have provided multispectral images over much larger areas than SAR at low cost. Due to such advantages, optical images have been widely used to measure the ice velocity of large glaciers and ice shelves in Antarctica (e.g., Stearns and Hamilton, 2005; Kaab et al., 2005; Scherler et al., 2008; Haug et al., 2010; Warner and Roberts, 2013), despite the clear disadvantages that images are unavailable during night and under cloudy conditions.

Most previous studies that evaluated ice velocities from the image matching of optical data used a single high-resolution band such as the panchromatic band of Landsat imagery (e.g., Haug et al., 2010; Heid and Kaab, 2012; Warner and Roberts, 2013). This is because matching correlations are largely dependent on the spatial resolution of images (Heid and Kaab, 2012; Noh and Howat, 2015). Although a high-resolution band produces a higher correlation than other lower resolution bands, many erroneous matches (i.e. mismatches) can be produced over glacial areas where visual contrast is relatively low. For better understanding of ice dynamics through image matching, it is required to obtain more correct matches in glacial areas. However, it is difficult to increase the number of correct matches based on a single image pair. Moreover, filtering of mismatches from a single band image pair is also difficult and remains a challenging field in image matching. The signal-to-noise ratio (SNR) and correlation coefficient of matches have been used to remove mismatches (Skvarca et al., 2003; Kääb, 2005; Kaab et al., 2005; Scherler et al., 2008; Warner and Roberts, 2013). However, as the SNR and correlation coefficient can vary depending on visual contrast and feature distribution, the use of user-specific thresholds for such indicators does not identify all mismatches and even removes some correct matches (Heid and Kaab, 2012). Several studies filtered mismatches using complicated processes including the manual extraction of glacial areas, investigation of ice flow direction, identification of a maximum displacement, and removal of the displacement fields that disagree with a certain criterion (Kääb, 2005; Kaab et al., 2005; Scherler et al., 2008; Heid and Kaab, 2012). Such filtering processes would leave some mismatches and thus require additional editing by manual investigation, which needs a lot of time and effort.

As the visual contrast of images over a glacier surface typically varies by spectral band, the ensemble of the image matching results of multiple spectral image pairs can provide more correct matches than using a single band image pair. Moreover, multiple matching results from various spectral image pairs can be complementary, which makes it easier and more effective to remove mismatches. This paper evaluates the variations in ice velocities of PIGIS using image matching of Landsat-7 ETM+ and Landsat-8 OLI time series multispectral data. The objectives of this research are to 1) measure the ice velocity of PIGIS using an ensemble of image matching results from the multispectral image pairs of Landsat imagery, 2) propose a robust but simple statistical method to filter the mismatches, and 3) investigate the spatiotemporal variations in ice velocities and surface strain rates on PIGIS. Section 2 presents the study area and data used in this study. Section 3 describes the methodology for image matching of Landsat multispectral data and the filtering process. Section 4 presents the results and discussion while Section 5 concludes this paper.

2. Study area and data

2.1. Pine Island Glacier Ice Shelf (PIGIS)

PIGIS (75°S, 102°W) is one of the largest ice shelves in the Amundsen Sea Embayment, West Antarctica (Fig. 1). PIGIS is composed of three ice shelves: a fast-flowing central ice shelf that is directly fed by PIG and two slow-moving ice shelves (northern and southern ice shelves) located on each side of the central ice shelf (Rignot, 2002). PIG and PIGIS drain a total area of ~175,000 km^2, corresponding to ~10% of the West Antarctic Ice Sheet, out to the ocean (Shepherd et al., 2001; Vaughan et al., 2006). The ice velocity of PIGIS increased from ~2.8 km a^{-1} in 1996 by ERS-1/2 InSAR (Mouginot et al., 2014) to ~4 km a^{-1} in 2012 measured by the speckle tracking of TanDEM-X SAR images (Mouginot et al., 2014). The total ice flux at the grounding line of PIG entering PIGIS increased from 78 ± 3 Gt a^{-1} to 132 ± 4 Gt a^{-1} over the last 40 years (Mouginot et al., 2014).

The mean ice thickness of freely floating areas of PIGIS decreased by ~6.8 m a^{-1} during 2003–2008 (Pritchard et al., 2012; Rignot et al., 2013), which was mainly caused by higher basal melting due to the strong circulation of circumpolar deep water (Bindschadler et al., 2011; Jacobs et al., 2011; Mankoff et al., 2012; Robertson, 2013; Rignot et al., 2014). The mass loss of PIGIS caused by basal melting was estimated as 101.2 ± 8 Gt a^{-1} during 2003–2008 (Rignot et al., 2013), which is 20 times larger than the surface accumulation over the ice shelf (4.6 ± 0.9 Gt a^{-1}) estimated from the Regional Atmospheric Climate Model (RACMO) surface mass balance model (Lenaerts et al., 2012). The grounding line of PIGIS retreated ~30 km at the glacier center from 1992 to 2011, while that of the side margins migrated ~10 km inland during the same period (Rignot et al., 2014).

2.2. Data

Landsat-7 ETM+ and Landsat-8 OLI data obtained from 2000 to 2014 (Table 1) were used to measure the ice velocities of PIGIS by image matching. Landsat satellites cover the Earth by a regular grid of locations called the World Reference System, which is composed of 233 orbits (paths) and 248 latitude points (rows). Overlapping ground coverage of

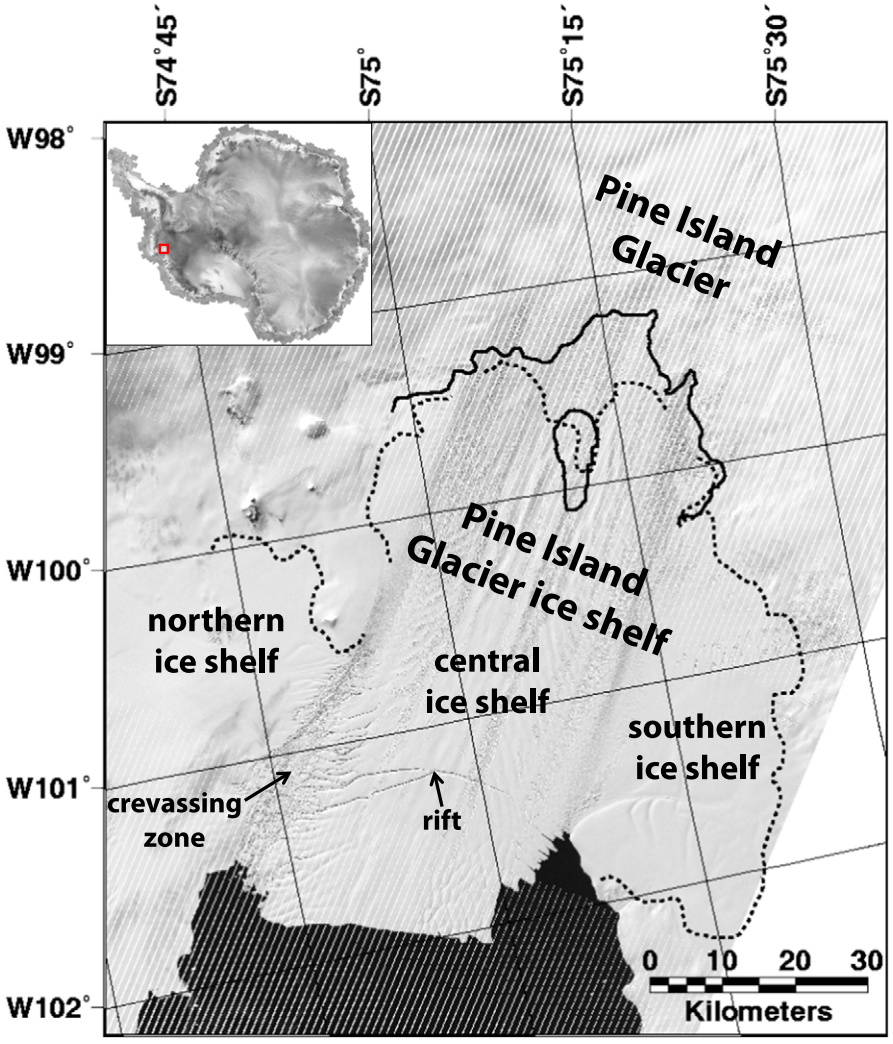

Fig. 1. Landsat-7 ETM + SLC-off panchromatic image of Pine Island Glacier Ice Shelf (PIGIS) obtained on 11 November 2012. The grounding line in 1999 is shown as the dotted lines (Rignot et al., 2011b), and that in 2009 is shown as the solid lines (Joughin et al., 2010). The white linear features over the image are caused by the failure of the Scan Line Corrector (SLC) on Landsat-7 ETM+.

the Landsat satellites widens with increasing latitude due to the convergence of the paths (Bindschadler, 2003). Three paths indexed as 1, 232, and 233 at row 113 cover PIGIS. The use of images from all available paths/rows over PIGIS enables more frequent observation of the ice shelf. In this study, Landsat multispectral data from the three coordinates of 1/113, 232/113 and 233/113 were used to perform image matching for PIGIS velocity measurement. All Landsat data were systematic terrain correction products (Level 1 GT) in polar stereographic projection.

The ice velocity of PIGIS measured by speckle tracking of TanDEM-X SAR images in November to December 2012 (Mouginot et al., 2014; Rignot et al., 2014), a part of the dataset derived from the NASA Making Earth System Data Records for Use in Research Environments (MEaSUREs) Program, was used to validate the results from Landsat image matching for the 2011–2012 image pair. The TanDEM-X ice velocity is composed of two-dimensional velocity fields with a grid size of 450 m. TanDEM-X SAR images have a very high resolution of ~1 m and thus the speckle tracking error is very small, less than 2 m (Rignot et al., 2014). As the TanDEM-X velocity fields represent the velocity later in 2012 (i.e., November to December), it cannot be exactly compared to the Landsat image matching results that represent an annual average of the ice velocity in 2012. Therefore, the validation results of the Landsat image matching using the TanDEM-X velocity fields were analyzed with the consideration of the different epochs between the two velocity datasets.

3. Methodology

Since the visual contrast of features on the ice surface varies by spectral band, the number of correct matches would also vary by spectral band. Therefore, the ensemble of matching results from individual spectral bands (hereafter referred to as the multispectral image matching) can provide more correct matches than when using a single band image pair. Fig. 2 illustrates the processing flow of the multispectral image matching of Landsat time series data.

3.1. Multispectral image matching based on orientation correlation

Image matching can be operated in both spatial and frequency domains. Normalized cross correlation (NCC) is a representative image matching method conducted in the spatial domain, which directly finds the position of the maximum of the cross correlations calculated using pixel values, i.e., digital numbers (DNs), within a matching window. Although NCC is very easy to use because of its simplicity, it might not be a good approach for measuring surface displacement in areas of low contrast such as snow covered glaciers (Heid and Kaab, 2012). It also produces many mismatches in the areas of data voids such as the gaps of Landsat-7 scan line corrector (SLC)-off data (Haug et al., 2010; Heid and Kaab, 2012). This is because the cross correlation

Table 1
Landsat-7 ETM + and Landsat-8 OLI data of Pine Island Glacier Ice Shelf (PIGIS) used in this study. The initial offsets in the image easting (x) and northing (y) directions were applied to the images of later dates before conducting image matching.

ID	Landsat sensor	Date	Path/row	Time difference (days)	Initial offsets in x and y direction (m)
1	ETM +	6 Mar 2000	1/113		
				304	−750, 1950
2	ETM +	4 Jan 2001	1/113		
3	ETM +	13 Jan 2001	233/113		
				336	−900, 2400
4	ETM +	15 Dec 2001	233/113		
				336	−900, 2400
5	ETM +	16 Nov 2002	233/113		
6	ETM +	28 Jan 2003	232/113		
				368	−1050, 2700
7	ETM +	31 Jan 2004[a]	232/113		
				368	−1050, 2700
8	ETM +	2 Feb 2005[a]	232/113		
9	ETM +	24 Jan 2005[a]	233/113		
				720	−2400, 6000
10	ETM +	14 Jan 2007[a]	233/113		
				672	−2100, 5400
11	ETM +	16 Nov 2008[a]	233/113		
12	ETM +	12 Jan 2009[a]	232/113		
				320	−900, 2400
13	ETM +	28 Nov 2009[a]	232/113		
				368	−1050, 2700
14	ETM +	1 Dec 2010[a]	232/113		
15	ETM +	8 Dec 2010[a]	233/113		
				384	−1050, 2700
16	ETM +	27 Dec 2011[a]	233/113		
				320	−900, 2400
17	ETM +	11 Nov 2012[a]	233/113		
18	OLI	1 Dec 2013	232/113		
				368	−1050, 2700
19	OLI	4 Dec 2014	232/113		

[a] SLC-off data.

computed in the spatial domain is dominated by the DNs within a matching window.

Image matching operated in the frequency domain calculates cross correlation by multiplying the Fourier transform of one image and the complex conjugate of the Fourier transform of the other image, which is faster than image matching in the spatial domain (Anuta, 1970; Kwok et al., 1990; Fitch et al., 2002; Haug et al., 2010; Heid and Kaab, 2012; Warner and Roberts, 2013). Orientation correlation (OC) (Fitch et al., 2002) using Fast Fourier transform (FFT) on directional derivatives of DNs shows the highest performance for the measurement of displacement fields over glaciers and ice shelves showing low visual contrast, compared to other image matching approaches such as NCC operated in the spatial domain or the phase correlation in the frequency domain (Haug et al., 2010; Heid and Kaab, 2012). Moreover, OC makes it possible to produce correct matches from the Landsat-7 ETM + SLC-off data because the frequency domain method is insensitive to the regular stripes of data voids which contribute to only a few frequencies and these areas are neglected in the image matching using the cross correlation of OC (Haug et al., 2010; Heid and Kaab, 2012). Based on such advantages, OC was implemented in this study to conduct image matching of Landsat multispectral data.

In order to perform OC, orientation images should be created from the directional derivative of DNs of the original images. Taking f as one image and g as the other image, the orientation images f_0 and g_0 are created by (Haug et al., 2010; Heid and Kaab, 2012):

$$f_0(x,y) = \mathrm{sgn}\left(\frac{\partial f(x,y)}{\partial x} + i\frac{\partial f(x,y)}{\partial y}\right),$$
$$g_0(x,y) = \mathrm{sgn}\left(\frac{\partial g(x,y)}{\partial x} + i\frac{\partial g(x,y)}{\partial y}\right), \quad (1)$$
$$\text{where } \mathrm{sgn}(x) = \begin{cases} 0 & \text{if } x = 0 \\ e^{i\arg x} & \text{otherwise} \end{cases}$$

where sgn is the signum function, i is the complex imaginary unit and arg is the complex argument function. The orientation images are complex, with the DN differences in the horizontal x direction as the real part and the DN differences in the vertical y direction as the imaginary part. The correlation surface ($P(x,y)$) is calculated as (Haug et al., 2010; Heid and Kaab, 2012):

$$P(x,y) = \mathrm{IFFT}\left(\frac{F_0(u,v)G_0^*(u,v)}{|F_0(u,v)G_0^*(u,v)|}\right) \quad (2)$$

where F_0 is the FFT of the reference window from f_0, G_0 is the complex conjugate of the FFT of the search window from g_0, and IFFT is the Inverse FFT. A displacement field (dx, dy) is found from the position showing the maximum $P(x,y)$ in a matching window. The subpixel displacements in the x (dx_s) and y (dy_s) directions are determined by fitting orthogonal parabolic functions to the correlations, which are found using (Argyriou and Vlachos, 2007):

$$dx_s = \frac{P(x_m+1,y_m) - P(x_m-1,y_m)}{2(2P(x_m,y_m) - P(x_m+1,y_m) - P(x_m-1,y_m))},$$
$$dy_s = \frac{P(x_m1,y_m+1) - P(x_m,y_m-1)}{2(2P(x_m,y_m) - P(x_m,y_m+1) - P(x_m,y_m-1))} \quad (3)$$

where $P(x_m,y_m)$ is the maximum correlation value. Fitting a parabolic curve to the correlation surface makes a narrower correlation peak, which results in better subpixel accuracy (Haug et al., 2010; Heid and Kaab, 2012). The subpixel displacements are added to the pixel level displacements (dx_0, dy_0) in order to find the complete displacement fields.

OC was conducted for the blue (B), green (G), red (R), near-infrared (NIR), panchromatic (Pan), and the first principal component (PC) image pairs of the Landsat multispectral data. The first PC accounts for the maximum proportion of variance in all the original bands. The two

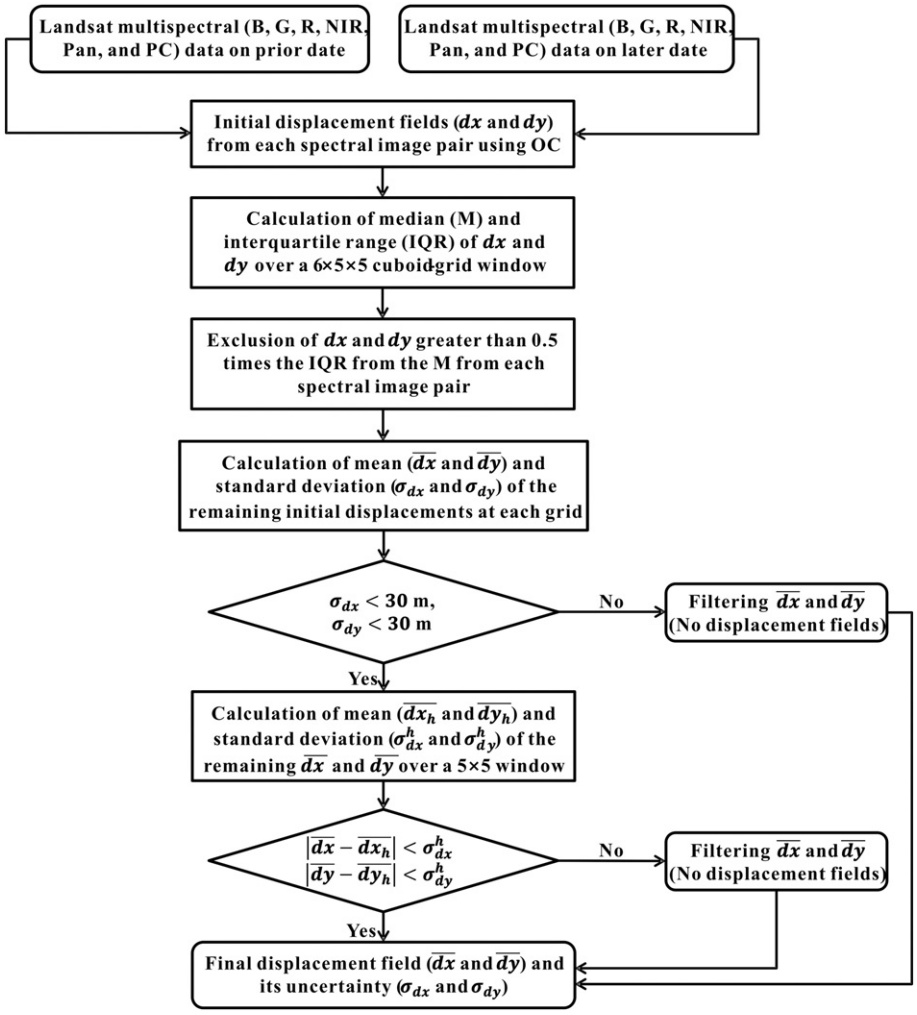

Fig. 2. Flowchart of the multispectral image matching of Landsat data proposed in this study.

shortwave infrared bands of the Landsat data were not used for the multispectral image matching because they are much more sensitive to snow cover properties, such as wetness, than the features on ice surfaces, such as crevasses (Bronge and Bronge, 1999; Racoviteanu et al., 2008). All image pairs were high-pass filtered to emphasize visual contrast before conducting image matching. The optimal sizes of reference and search windows that are big enough to contain surface features but small enough to limit velocity gradients should be selected to conduct image matching successfully. A reference window size of 64 × 64 pixels pixels and a search window size of 256 × 256 pixels were used in the image matching of both the Pan and the other bands. The displacement measured by the image matching operated in the frequency domain cannot be larger than half the window size because the Fourier spectrum of a window is divided in four equal quadrants (Heid and Kaab, 2012). To measure high ice velocity in the given window size, initial offsets in the image easting (horizontal *x* direction) and northing (vertical *y* direction) directions were applied to the image of a later date (Table 1). The reference window size of 64 × 64 pixels corresponds to a 960 × 960 m at the Pan band and a 1920 × 1920 m at the other bands, respectively. The reference windows were overlapped during the image matching to generate displacement fields as a grid of 480 × 480 m.

3.2. Mismatch filtering process

Raw matching results typically contain a large number of erroneous matches. In this study, an objective and automated filtering method (Fig. 2) is proposed to remove mismatches of the raw matching results produced from the Landsat spectral image pairs. The filtering method uses two assumptions: 1) individual spectral image pairs produce the same displacement field in the same area, and 2) glacier flows have smooth spatial variations. First, the median and interquartile range of the displacement fields in both the image easting and northing directions over a 6 × 5 × 5 cuboid-grid window (i.e. 5 × 5 horizontal grids in 6 spectral image pairs) are computed. For both directions, the displacement fields greater than 0.5 times the interquartile range from the median are regarded as erroneous fields based on the above assumptions, and thus are excluded from the raw matching results for each spectral image pair. Then the mean ($\overline{dx}$ and $\overline{dy}$) and standard deviation (σ_{dx} and σ_{dy}) in the spectral domain are computed at each displacement grid using the remaining displacement fields.

The values of σ_{dx} and σ_{dy} computed for the remaining displacement fields include the errors from the displacement measurement by the OC method, and image-to-image and band-to-band registration errors of the Landsat multispectral data. Haug et al. (2010) evaluated the accuracy of the subpixel displacement measurement by OC to be approximately 1/4 pixel which corresponds to ~7.5 m for the Landsat multispectral data. The image-to-image registration error of both the Landsat-7 ETM+ and Landsat-8 OLI is less than 12 m (Lee et al., 2004; Storey et al., 2014). The errors from band-to-band registration are ~8 m for the Landsat-7 ETM+ and ~5 m for the Landsat-8 OLI (Lee et al., 2004; Storey et al., 2014). A combination of such errors is smaller than the pixel size of the Landsat multispectral data. Therefore, the mean displacement fields ($\overline{dx}$ and $\overline{dy}$) of σ_{dx} and σ_{dy} larger than 30 m were

excluded and considered as no displacement fields to the final displacement fields. Finally, a neighbor filter was applied to the $\overline{dx}$ and $\overline{dy}$ fields using the mean ($\overline{dx}_h$ and $\overline{dy}_h$) and standard deviation (σ^h_{dx} and σ^h_{dy}) over a 5 × 5 neighboring fields. The $\overline{dx}$ and $\overline{dy}$ vectors that deviate more than σ^h_{dx} and σ^h_{dy} from $\overline{dx}_h$ and $\overline{dy}_h$, respectively, were removed resulting in no displacement fields. The remaining $\overline{dx}$ and $\overline{dy}$ vectors were used to produce the final velocity fields.

The flow-oriented surface strain rates, such as longitudinal ($\dot{\varepsilon}_l$), transverse ($\dot{\varepsilon}_t$) and shear strain rate ($\dot{\varepsilon}_s$), were calculated from the final velocity fields by (Bindschadler et al., 1996):

$$\begin{aligned}\dot{\varepsilon}_l &= \dot{\varepsilon}_{xx}\cos^2\alpha + 2\dot{\varepsilon}_{xy}\sin\alpha\cos\alpha + \dot{\varepsilon}_{yy}\sin^2\alpha \\ \dot{\varepsilon}_t &= \dot{\varepsilon}_{xx}\sin^2\alpha - 2\dot{\varepsilon}_{xy}\sin\alpha\cos\alpha + \dot{\varepsilon}_{yy}\cos^2\alpha \\ \dot{\varepsilon}_s &= (\dot{\varepsilon}_{yy} - \dot{\varepsilon}_{xx})\sin\alpha\cos\alpha + \dot{\varepsilon}_{xy}\left(\cos^2\alpha - \sin^2\alpha\right)\end{aligned} \quad (4)$$

where $\dot{\varepsilon}_{xx}$, $\dot{\varepsilon}_{yy}$, and $\dot{\varepsilon}_{xy}$ are the strain rates with respect to the image easting and northing directions, and α is the flow direction measured counter clockwise from the image easting direction.

4. Results and discussion

4.1. Validation of the multispectral image matching

The performance of the Landsat single band image matching using OC was evaluated prior to validating the multispectral image matching. For the 2011–2012 Landsat spectral image pairs (ID 16 and 17 in Table 1), the ice velocity magnitudes were converted from the displacement fields filtered by the mismatch filtering method proposed by Heid and Kaab (2012). Heid and Kaab (2012) filtered the displacement fields in both the image easting and northing directions that deviate more than ±150 m from their 3 × 3 mean low-pass filtered displacement field. Fig. 3 shows the difference between the velocity magnitudes from the individual 2011–2012 Landsat multispectral image pairs and the 2012 TanDEM-X SAR images, as a ratio of the TanDEM-X velocity magnitude. The spatial coverage of the potential correct matches varies by the spectral band due to the different visual contrast. The image matching result from the panchromatic band provided more potentially correct matches on the uppermost part of the central ice shelf more than the other spectral bands, while it could not completely provide ice velocity from ~10 km downstream of the 1999 grounding line to the ice

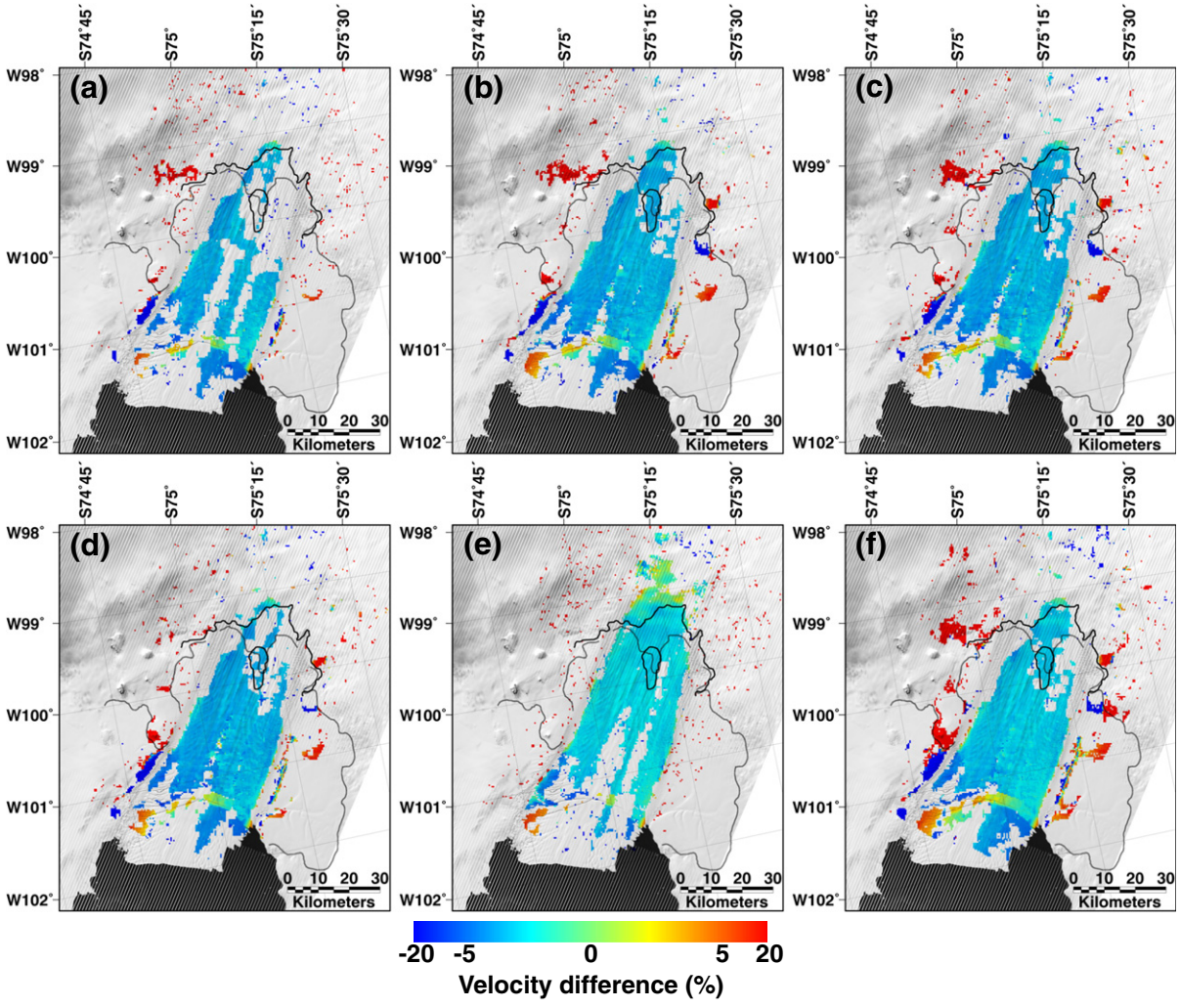

Fig. 3. The differences between the velocity magnitudes of PIGIS from the 2011–2012 Landsat multispectral image pairs and the 2012 TanDEM-X SAR images (i.e., Landsat velocity minus TanDEM-X velocity), as a ratio to the TanDEM-X velocity magnitude (note the nonlinear color scale). The image matching results from the Landsat image pairs of (a) B, (b) G, (c) R, (d) NIR, (e) Pan, and (f) PC were filtered using the mismatch filtering process described in Heid and Kaab (2012). The Landsat ETM + panchromatic image obtained on 11 November 2012 was used as a background image. The grounding line in 1999 is shown as the dotted lines (Rignot et al., 2011b), and that in 2009 is shown as the solid lines (Joughin et al., 2010).

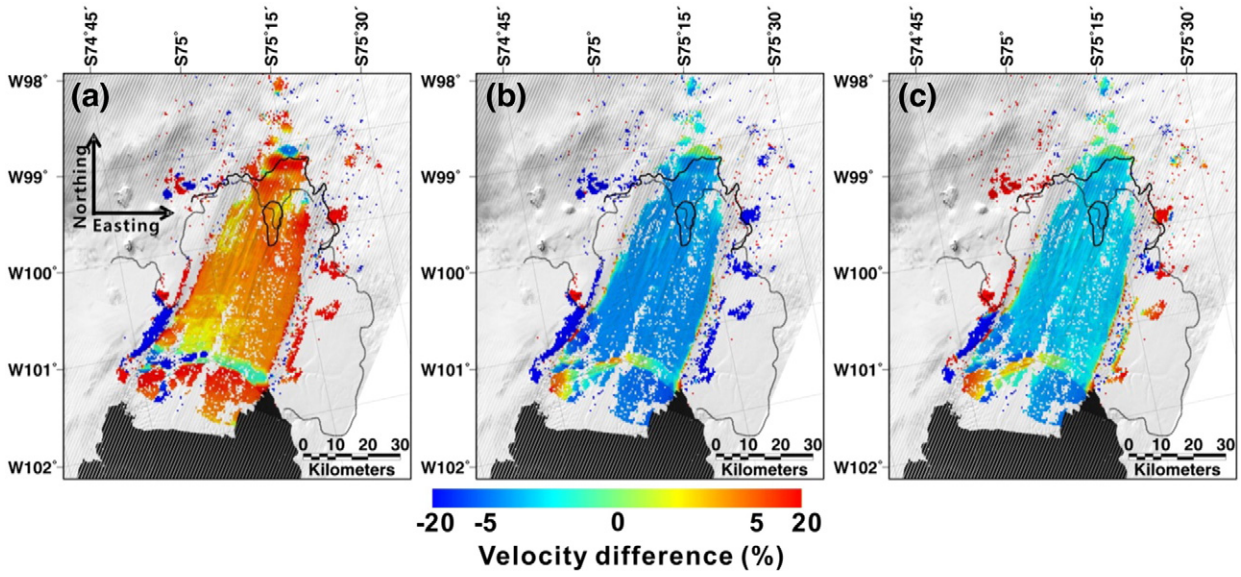

Fig. 4. The differences between the final velocity fields of PIGIS from the 2011–2012 Landsat multispectral image matching and the 2012 TanDEM-X SAR images (i.e., Landsat velocity minus TanDEM-X velocity), as a ratio to the TanDEM-X velocity fields (note the nonlinear color scale). The differences of ice velocities were computed for (a) the image easting component, (b) the image northing component, and (c) magnitude. The Landsat ETM+ panchromatic image obtained on 11 November 2012 was used as a background image. The grounding line in 1999 is shown as the dotted lines (Rignot et al., 2011b), and that in 2009 is shown as the solid lines (Joughin et al., 2010).

calving front (Fig. 3e). Meanwhile, image pairs of visible bands except for B, NIR, and PC provided the ice velocity from the isolated grounding line in 2009 to the rifting zone near the ice calving front, but not near the uppermost part of the central ice shelf (Fig. 3a–d and f). This implies that synergistic combination of the image matching results from multiple spectral bands can provide more correct matches than the use of single band image matching.

In Fig. 3, it is shown that the TanDEM-X velocities are systematically faster than the Landsat velocities in the fast-flowing areas of the central ice shelf of PIGIS, representing that an annual average of the ice velocity in 2012 was slower than the ice velocity later in 2012 (i.e., November to December). However, the velocity differences in the fast-flowing areas are no greater than −4%. Landsat velocities much faster than the TanDEM-X velocities were observed on the geographically northern side of the downstream of a massive rift near the ice front of the central ice shelf (as shown in Fig. 1) and in a narrow band that extends halfway across the ice shelf along the rift. The perimeter of the central ice shelf also showed faster Landsat velocities than the TanDEM-X velocities. Meanwhile, the TanDEM-X velocities were considerably faster in a narrow band of the upstream of the rift on the geographically northern side of the ice shelf and the southern side of the downstream of the rift. Such large differences were attributed to either the different epochs or sources of the two velocity datasets, or the remaining mismatches in the filtered Landsat velocity fields. The different spatial resolutions and image matching methods between the two datasets can produce a slightly different velocity field over the same area (Debella-Gilo and Kaab, 2011; Debella-Gilo and Kaab, 2012). The epochs of the TanDEM-X velocity fields from Mouginot et al. (2014) were from November to December 2012, which is an approximately 6-month time difference from the middle of the Landsat image pair that represents an annual average of ice velocity in 2012. Such different epochs can contribute to the large differences in the ice velocities depending on a possible annual or seasonal variation of ice flow of the PIGIS. The different time intervals of the Landsat and TanDEM-X image pairs also contributed to the velocity differences. As the velocities were measured from the displacements at the location of the reference windows, the Landsat velocities for about a year are shifted slightly upstream when considering PIGIS velocities of several kilometers per year (Warner and Roberts, 2013; Mouginot et al., 2014). Since TanDEM-X velocities were measured from the shorter time interval of the image pairs than the Landsat velocities, they are less affected by the issue of the epoch duration. Therefore, the longer time interval between the Landsat image pairs would result in a small systematic bias in the comparison of the Landsat and TanDEM-X velocities. In particular, the large differences near the rift could be mainly attributed to the different epochs and time intervals of image pairs used in image matching between the two velocity datasets. In October 2011, a newly formed rift near the ice front of the central ice shelf was discovered by aircraft survey (Jones and Gudmundsson, 2014). The rift propagated from the geographically northern margin to the southern part of the central ice shelf of PIGIS (Fig. 1) and completely separated the ice shelf in November 2013. The evolution of the rift would have different effects on the ice velocities across the ice shelf around the rift as captured by the two epochs. The opening of the rift might bring about rotations of the downstream ice block (Joughin and MacAyeal, 2005; Glasser and Scambos, 2008), which would increase the displacements in the narrow band across the ice shelf along the rift during the Landsat observations, while the separation on the southern side later in 2012 might result in increased displacements on the geographically southern side of the downstream of the rift in the TanDEM-X epoch. The TanDEM-X velocities much faster than the Landsat velocities localized on the upstream of the rift on the geographically northern part of the ice shelf were probably due to the increased velocity at the open rift compared to the flow for the annual average of the region. The systematic bias in the comparison of Landsat and TanDEM-X velocities, attributed to the

Fig. 5. The ice velocity fields of PIGIS in 2000 (left column) and 2014 (right column) obtained from the Landsat multispectral image matching. (a, b) The image easting velocity component (a black line in each color bar represents a zero velocity-mark); (c, d) the image northing velocity component (note the nonlinear color scale); and (e, f) the velocity magnitudes (note the nonlinear color scale). Note the different color scales of the velocities between 2000 and 2014. The Landsat-7 ETM+ SLC-off panchromatic image obtained on 4 January 2001 and the Landsat-8 OLI panchromatic image obtained on 4 December 2014 were used as the background images of the 2000 and 2014 velocity fields, respectively. The arrows on (e) and (f) represent the local flow direction. The grounding line in 1999 is shown as the dotted lines (Rignot et al., 2011b), and that in 2009 is shown as the solid lines (Joughin et al., 2010). The red dotted line in (a) is the profile of the velocity variations as shown in Fig. 7.

different time intervals of image pairs in velocity measurements, would presumably be emphasized near the rift where ice velocity would be much faster than other regions of PIGIS. Therefore, the large discrepancies in ice velocities near the rift would be caused by the different epochs and time intervals of image pairs of the velocity field between the Landsat that represents for an annual average in 2012

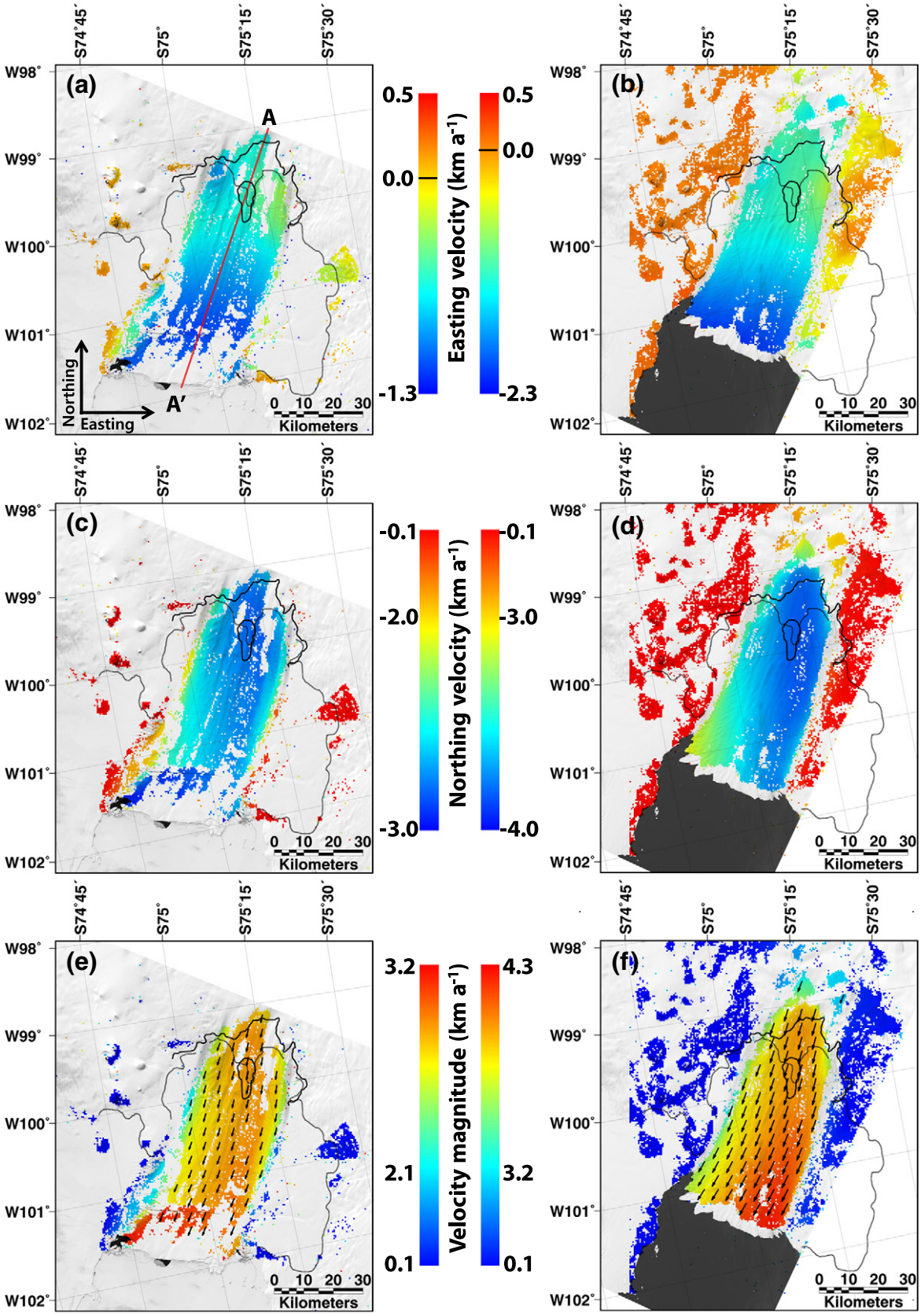

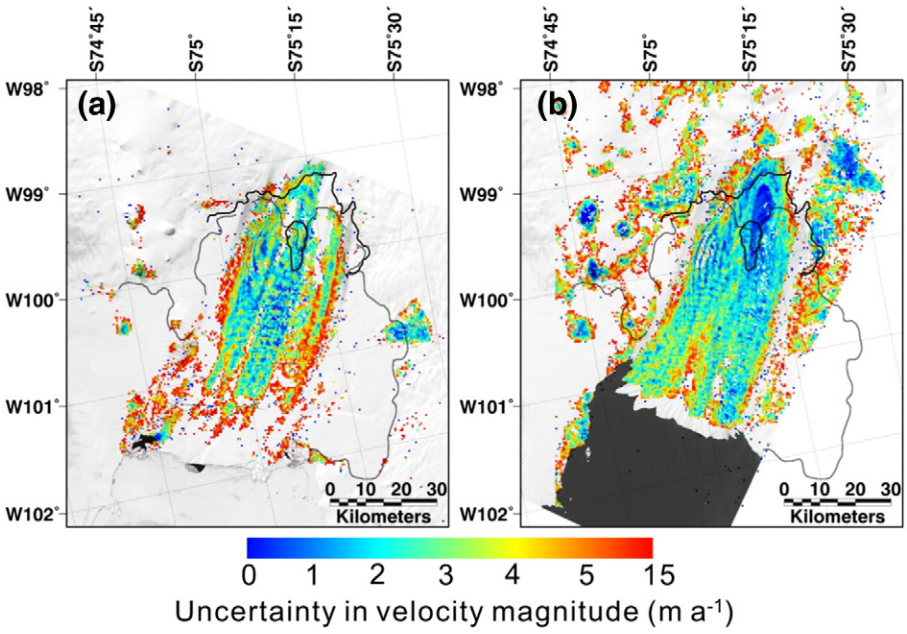

Fig. 6. Uncertainties in the velocity magnitudes of PIGIS in (a) 2000 and (b) 2014 obtained from the Landsat multispectral image matching (note the nonlinear color scale). The Landsat-7 ETM + SLC-off panchromatic image obtained on 4 January 2001 and the Landsat-8 OLI panchromatic image obtained on 4 December 2014 were used as the background images of the 2000 and 2014 velocity fields, respectively. The grounding line in 1999 is shown as the dotted lines (Rignot et al., 2011b), and that in 2009 is shown as the solid lines (Joughin et al., 2010).

incorporating the period of rift growth and that from the TanDEM-X representing later in 2012 (i.e., November to December). However, any large differences caused by erroneous Landsat velocity fields cannot be clearly examined from the single band image matching. Using a statistical filtering process of the multispectral image matching results enables a more detailed interpretation of the velocity.

The multispectral image matching and the mismatch filtering method proposed in this research were applied to the time series Landsat data. Fig. 4 depicts the differences between the final velocity fields from the 2011–2012 Landsat multispectral image matching and late 2012 TanDEM-X SAR velocity fields. The differences in the image easting and northing velocity components were ~5% (Fig. 4a) and ~−5% (Fig. 4b), respectively, except for the ice calving front of the central ice shelf of PIGIS. This suggests that the image northing velocity components were enhanced in late 2012 compared to the annual average for the components, while the image easting velocity components slowed down. The differences in the velocity magnitudes (Fig. 4c) were similar to those in the image northing velocity components (Fig. 4b) because the ice flow of the central ice shelf is primarily driven by the image northing component (Warner and Roberts, 2013), except for the geographically southern margin and the perimeter of the ice shelf where the dominant component of ice flow is the image easting velocity.

Although the erroneous displacement fields included in the individual spectral image pairs were removed using statistically rigorous evaluations, large differences in the velocity fields were still observed near the ice calving front and the perimeter of the central ice shelf. The large differences observed near the perimeter of the central ice shelf were probably caused by the different epochs and sources between the Landsat and TanDEM-X velocity datasets. The velocity magnitudes on the perimeter of the central ice shelf of PIGIS are typically less than 150 m a^{-1}. Therefore, a slightly different velocity measured from a different source could cause the large proportional velocity deviations on the perimeter of the central ice shelf. Large disagreements between the Landsat and TanDEM-X velocity fields were observed along the massive rift near the ice front (as shown in the underlying panchromatic image in 2012 of Fig. 4) and a narrow band localized on the upstream of the rift on the geographically northern part of the ice shelf. As discussed above regarding Fig. 3, such large differences near the rift would be caused by the different epochs between the two velocity datasets.

The final velocity fields from the Landsat multispectral image matching covered PIGIS ~35% more than the single band (i.e., panchromatic) image matching. Meanwhile, the erroneous displacement fields produced from the individual spectral image pairs were mostly removed by the statistical filtering process. Consequently, it is concluded that multispectral image matching can provide reasonable velocity fields with more complete coverage than single band image matching, by removing mismatches easily using an objective and automated filtering process.

4.2. Variations in ice velocities of the Pine Island glacier ice shelf (PIGIS)

Ice velocities of PIGIS from 2000 to 2014 were measured by Landsat multispectral image matching. The ice velocities in the image easting and northing directions, and velocity magnitudes of PIGIS in 2000 (from ID 1 and 2 in Table 1) and 2014 (from ID 18 and 19 in Table 1) are shown in Fig. 5. The Landsat-7 ETM + panchromatic image obtained on 4 January 2001 and the Landsat-8 OLI panchromatic image on 18 October 2014 were used as the background images of the velocities in 2000 and 2014, respectively. The black arrows in Fig. 5e and f represent the ice flow direction. Note that color scales of ice velocities in 2000 are different from those in 2014 in order to present the spatiotemporal variation of the velocities in the central ice shelf. Ice velocities in the image easting and northing directions of the entire PIGIS in 2014 (Fig. 5b and d) were much faster than those in 2000 (Fig. 5a and c). The velocities in both 2000 and 2014 showed that the image easting components gradually increased in magnitude from the grounding line to the ice front along the flow lines (Fig. 5a and b), while the image northing components increased in magnitude from the shear margins to the central flow line (Fig. 5c and d). Ice velocities in the image northing component in the geographically southern part of the central ice shelf were faster than those in the northern part of the ice shelf. The spatial variations of the velocity magnitude of the central ice shelf of PIGIS (Fig. 5e and f) were similar to those of the velocity component in the image northing direction (Fig. 5c and d) because the ice flow is primarily driven by the

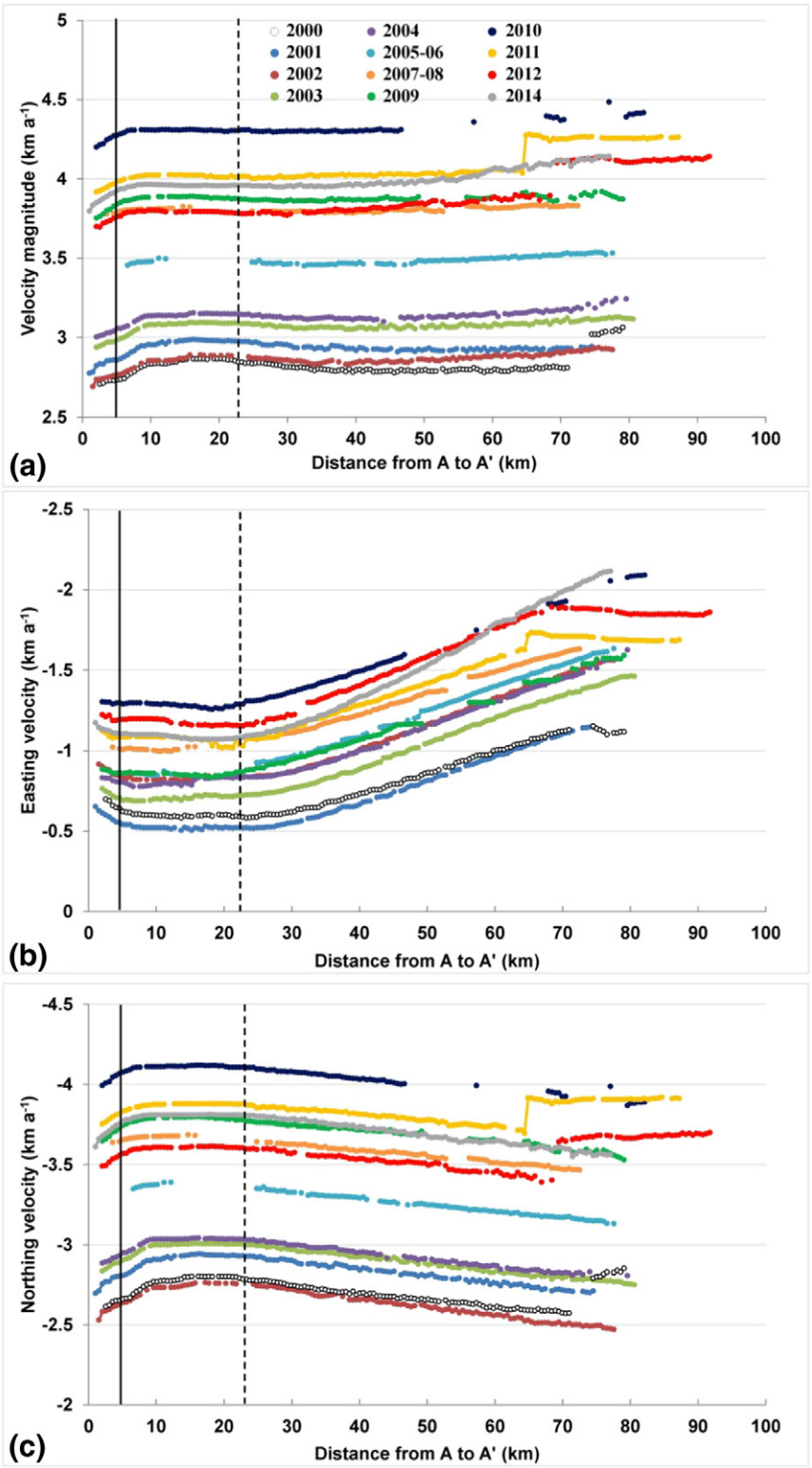

Fig. 7. The ice velocity profiles of the central ice shelf of PIGIS during 2000–2014 along the profile marked as A–A′ in Fig. 5(a). (a) The velocity magnitudes; (b) the image easting velocity components; and (c) the image northing velocity components. The vertical dotted line represents the location of the grounding line in 1999 (Rignot et al., 2011b), and the vertical solid line represents the grounding line in 2009 (Joughin et al., 2010).

image northing component (Warner and Roberts, 2013). The velocity magnitude and the image northing velocity component in 2000 (Fig. 5c and e) showed that the flow of the ice front was much faster than other areas of the central ice shelf. Such a fast motion near the ice front was once again caused by a rift (as shown in the underlying panchromatic image in 2000) that decoupled the ice front from the body of the ice shelf.

Uncertainties in the velocity magnitudes from the Landsat multispectral image matching were estimated by combining the uncertainties in the image easting and northing velocity components, i.e.,

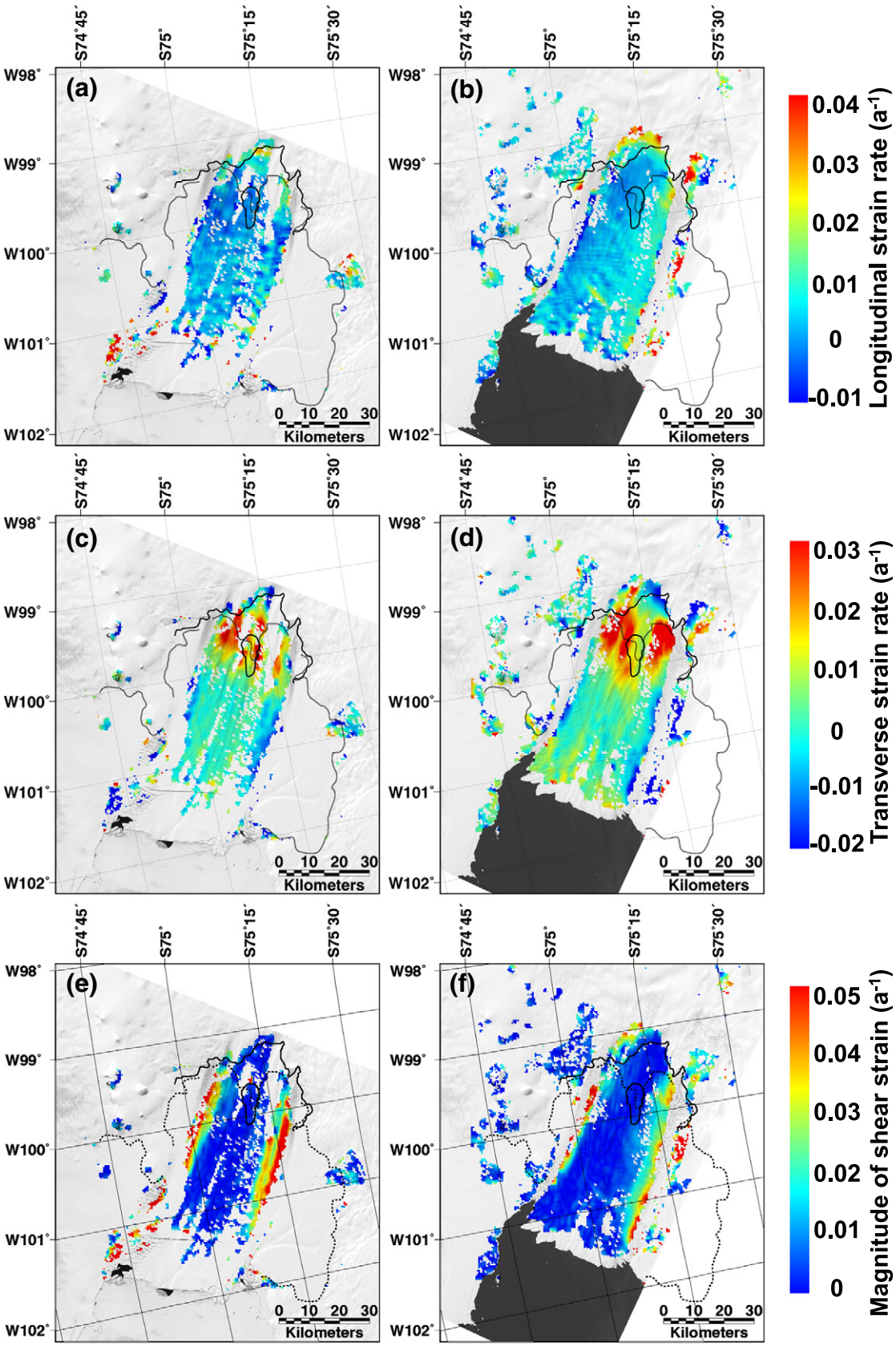

Fig. 8. Surface strain rates of PIGIS in 2000 (left column) and 2014 (right column) derived from the final velocity fields of the Landsat multispectral image matching. (a, b) The longitudinal strain rate; (c, d) the transverse strain rate; and (e, f) the magnitude of the aligned shear strain rate. The Landsat-7 ETM + SLC-off panchromatic image obtained on 4 January 2001, and the Landsat-8 OLI panchromatic image obtained on 4 December 2014 were used as the background images of the 2000 and 2014 strain rates, respectively. The grounding line in 1999 is shown as the dotted lines (Rignot et al., 2011b), and that in 2009 is shown as the solid lines (Joughin et al., 2010).

σ_{dx} and σ_{dy}. The uncertainties in the 2000 and 2014 Landsat velocity magnitudes are shown in Fig. 6a and b, respectively. The uncertainties for the 2000 velocity magnitude were less than 5 m a^{-1} in the central ice shelf of PIGIS, except for margins and the downstream of rift of the ice shelf in 2000 in which the uncertainties were estimated as ~15 m a^{-1}. Meanwhile, most uncertainties for the 2014 velocity magnitude were ~2.5 m a^{-1} in the central ice shelf, but some larger uncertainties were produced near margins and ice front of the ice shelf. Uncertainty of 5 m a^{-1} corresponds to 0.17% of the 2000 velocity magnitudes, while that of 2.5 m a^{-1} corresponds to 0.06% of the 2014 velocity magnitudes. As the uncertainties in the image easting and northing velocity components were approximately equal in both 2000 and 2014, uncertainty in each velocity component was approximately 70% of the uncertainty in the velocity magnitude.

Variations in the velocity magnitudes, and the image easting and northing velocity components of the central ice shelf of PIGIS from 2000 to 2014 along the profile marked as A–A′ in Fig. 5(a) are shown in Fig. 7. The velocity magnitudes of the whole central ice shelf accelerated by ~1.5 km a^{-1} (or ~55%) between 2000 and 2010, and then decelerated by ~0.5 km a^{-1} (or ~10%) from 2010 to 2012 (Fig. 7a), which agrees with the previous research findings (Rignot et al., 2002; Warner and Roberts, 2013; Mouginot et al., 2014). The velocity magnitudes in 2000, 2011, and 2012 suddenly increased from ~70 km downstream of the 1999 grounding line, which was caused by widespread rifting. The sudden increases in the ice velocity in 2011 and 2012 were due to the same rift that propagated across the ice shelf from October 2011 to November 2013, while those in 2000 were caused by an earlier rift that cut the ice shelf and produced a huge iceberg in 2001.

The velocity magnitudes in 2014 were ~0.2 km a^{-1} higher than those in 2012. The ice velocity of PIGIS in 2013 was not measured in this study due to the lack of cloud-free Landsat data. Mouginot et al. (2014) reported that PIGIS decelerated between 2010 and 2013, from which it can be deduced that the central ice shelf of PIGIS picked up speed again after 2013. While the velocity magnitudes increased slightly between 2012 and 2014, those values are still below the values reached in 2010. A temporary regrounding on the isolated grounding line mapped in 2009 (Joughin et al., 2010) could be a possible reason for the slow-down and partial reacceleration of PIGIS. However, there is no further investigation on the changes in the grounding line position of PIGIS after 2011, including the isolated grounding line. To clarify whether the isolated grounding line influences the changes in the ice velocity, it is necessary to keep investigating the grounding lines of PIGIS.

The magnitude of the velocity component in the image easting direction (Fig. 7b) increased by ~0.8 km a^{-1}, or ~70%, from 2000 to 2010. Between 2010 and 2014, the magnitude of the image easting velocity component near the grounding line slowed down by ~0.2 km a^{-1} (or ~17%). However, the ice front showed few temporal changes in the image easting velocities after 2010. The spatial variations in the image easting velocity component near the grounding line were very small because the ice flow in this area was primarily driven by the inflow of PIG, the direction of which was almost parallel to the image northing direction (Fig. 5e and f). Meanwhile, the magnitude of the image easting velocities increased rapidly from the grounding line to the ice front, which was due to the shear forces at the edge of the ice shelf (Rignot, 2002; MacGregor et al., 2012) and the inflow from the southern ice shelf.

The spatiotemporal variations of ice velocities in the image northing direction of the central ice shelf (Fig. 7c) were similar to those of the velocity magnitudes (Fig. 7a) because they were the dominant components of the flow speed of PIGIS (Warner and Roberts, 2013). During 2000–2010, the magnitude of the image northing velocity component of the central ice shelf accelerated by ~1.3 km a^{-1} (or ~50%), which was higher than the acceleration of the image easting velocity component during the same period (~0.8 km a^{-1}). The magnitude of the image northing velocity component slowed down by ~0.5 km a^{-1} (or ~12%) during 2010–2012. The magnitude of the image northing velocity component in 2014 was ~0.2 km a^{-1} faster than that in 2012, but this was still lower than the pattern of image northing velocities in 2010.

4.3. Variations in strain rate of the Pine Island Glacier Ice Shelf from 2000 to 2014

Surface strain rates of PIGIS in 2000 and 2014 calculated from Eq. (4) are shown in Fig. 8. The surface strain rates of PIGIS have largely been steady since 2000, except for a few regions showing noteworthy changes. The longitudinal strain rate (Fig. 8a and b) represents the extension (a positive value) or compression (a negative value) of ice flow along the local flow direction. The uppermost part (near the grounding line in 2009) and the geographically northern part of the central ice shelf of PIGIS showed negative longitudinal strain rate values of ~−0.01 a^{-1} in both 2000 and 2014, which implies ice was compressed along flow in this area during both epochs. Meanwhile, the geographically southern part of the ice shelf showed increasing longitudinal strain rates from −0.01 a^{-1} in 2000 to 0.01 a^{-1} in 2014 (around W 100–101°, S 75°15′), indicating development of a fast-flowing band of ice (Warner and Roberts, 2013). The geographically northern margin near the side of the central ice shelf front (around S74°35′, W101°) showed a very large longitudinal strain rate exceeding 0.04 a^{-1} (Fig. 8a), indicating large-scale extending deformations such as heavy crevassing, as shown in the underlying panchromatic image.

The transverse strain rates of PIGIS in 2000 and 2014 are shown in Fig. 8(c) and (d), respectively. A positive value of the transverse strain rate represents the divergence of the local ice flow whereas a negative value indicates ice convergence. Large positive transverse strain rates exceeding 0.03 a^{-1} were observed near the grounding line of the central ice shelf of PIGIS. This diverging ice flow was caused by the extending width of the ice flow in the hinge zone (Warner and Roberts, 2013). Such ice divergence in the hinge zone was enhanced and extended to ~15 km downstream (Fig. 8d) in 2014, which was possibly influenced by the central isolated grounded region found in 2009. The ice front of the central ice shelf showed the positive transverse strain rates of ~0.01 (Fig. 8d), indicating that the ice front underwent diverging flow. This is because the ice spread out into the ocean, by which numerous ice calving events have occurred in this region.

The magnitudes of the aligned shear strain rate along both sides of the central ice shelf of PIGIS exceeded 0.05 a^{-1} but those in the rest of the ice shelf were close to zero (Fig. 8e and f). This implies that the central ice shelf of PIGIS flowed very fast, experiencing lateral drag along the shear margins. The width of the shear margins of the central ice shelf was measured as ~25 km, and it has been stable since 2000. The heavy crevassing zone at the geographically northern margin near the side of the central ice shelf front (around S74°35′, W101°) showed a large magnitude of the shear strain rate (Fig. 8e), which indicates that the crevasses in the region were formed by both the largely extending and shearing flows.

Uncertainties of the surface strain rates are a function of uncertainties in the image easting and northing velocity components that were derived from mismatch filtering of the Landsat multispectral image matching. The uncertainties in each velocity component for the 2000 and 2014 Landsat velocity fields were typically ~3.5 m a^{-1} and ~2 m a^{-1}, respectively, which produced uncertainties in the strain rates with respect to the image easting and northing directions of approximately 0.01 a^{-1} and 0.006 a^{-1}, respectively. The resultant uncertainty in the flow-oriented surface strain rates would be greater than that in the component strain rates in image directions and this needs to be considered when interpreting the apparent variations in calculated surface strain rates, especially for the areas showing low strain rates. This is a limitation of measuring surface strain rates from image matching techniques. The uncertainties would be further reduced by taking local spatial averages over coherent regions of strain rates. Therefore, the surface strain rates for the freely floating part of

the central ice shelf where very low strain rates were measured should be interpreted with regard to the uncertainties, although they are comparable with the corresponding strain rates estimated by Warner and Roberts (2013).

5. Conclusion

Ice velocities of PIGIS were measured from an ensemble of image matching of Landsat-7 ETM + and Landsat-8 OLI multispectral data obtained from 2000 to 2014. Orientation correlation was adopted for the image matching of the individual Landsat spectral bands, from which the matching results were combined, except for the two shortwave infrared bands which produced few correct matches. The multispectral image matching provided more correct matches than the single band (i.e. panchromatic) image matching, and filtered out erroneous matches based on an objective and automated filtering approach.

The ice velocity of the central ice shelf of PIGIS accelerated from 2000 to 2010, when the acceleration of the image northing velocity component was higher than that of the image easting component. The central ice shelf velocity slowed down from 2010 to 2012. The ice velocities sped up after 2012, but in 2014 were still lower than the corresponding values in the peak of 2010. The surface strain rate fields of PIGIS were derived from the ice velocity fields measured by the multispectral image matching, which demonstrated that ice divergence in the hinge zone has increased since 2000. The longitudinal compression of ice was observed near the grounding line and the geographically northern part of the central ice shelf of PIGIS, while a fast-flowing band of ice was observed along the southern part of the ice shelf. The width of the shear margins of the ice shelf was ~25 km, which has been stable during the last 15 years.

This study showed that an ensemble of image matching results from multispectral image pairs can be very useful to evaluate the ice velocity of glaciers and ice shelves. We expect that the proposed multispectral image matching method can be adopted for the Sentinel-2 Multi-Spectral Imager, providing a continuity of glaciological applications of the Landsat satellite series.

Acknowledgements

This research was a part of the project titled 'SaTellite remote sensing on west Antarctic ocean Research (STAR) (KOPRI, PE16040)', funded by the Korea Polar Research Institute, South Korea.

References

Ahn, Y., Howat, I.M., 2011. Efficient automated glacier surface velocity measurement from repeat images using multi-image/multichip and null exclusion feature tracking. IEEE Trans. Geosci. Remote Sens. 49 (8), 2838–2846.
Anuta, P.E., 1970. Spatial registration of multispectral and multitemporal digital imagery using fast Fourier transform techniques. IEEE Trans. Geosci. Electron. GE-8 (4), 353–368.
Argyriou, V., Vlachos, T., 2007. Quad-tree motion estimation in the frequency domain using gradient correlation. IEEE Trans. Multimedia 9 (6), 1147–1154.
Bindschadler, R., 2003. Landsat coverage of the earth at high latitudes. Photogramm. Eng. Remote. Sens. 69 (12), 1333–1339.
Bindschadler, R., Vornberger, P., Blankenship, D., Scambos, T., Jacobel, R., 1996. Surface velocity and mass balance of Ice Streams D and E, West Antarctica. J. Glaciol. 42 (142), 461–475.
Bindschadler, R., Vaughan, D.G., Vornberger, P., 2011. Variability of basal melt beneath the Pine Island Glacier ice shelf, West Antarctica. J. Glaciol. 57 (204), 581–595.
Bronge, L.B., Bronge, C., 1999. Ice and snow-type classification in the Vestfold Hills, East Antarctica, using Landsat-TM data and ground radiometer measurements. Int. J. Remote Sens. 20 (2), 225–240.
De Angelis, H., Skvarca, P., 2003. Glacier surge after ice shelf collapse. Science 299 (5612), 1560–1562. http://dx.doi.org/10.1126/science.1077987.
Debella-Gilo, M., Kaab, A., 2011. Sub-pixel precision image matching for measuring surface displacements on mass movements using normalized cross-correlation. Remote Sens. Environ. 115, 130–142.
Debella-Gilo, M., Kaab, A., 2012. Measurement of surface displacement and deformation of mass movements using least squares matching of repeat high resolution satellite and aerial images. Remote Sens. 4 (1), 43–67.
Dupont, T.K., Alley, R.B., 2005. Assessment of the importance of ice-shelf buttressing to ice-sheet flow. Geophys. Res. Lett. 32, L04503. http://dx.doi.org/10.1029/2004GL022024.
Fitch, A.J., Kadyrov, A., Christmas, W.J., Kittler, J., 2002. Orientation correlation. British Machine Vision Conference, pp. 133–142.
Forster, R.R., Jezek, K.C., Koenig, L., Deeb, E., 2003. Measurement of glacier geophysical properties from InSAR wrapped phase. IEEE Trans. Geosci. Remote Sens. 41 (11), 2595–2604.
Glasser, N.F., Scambos, T.A., 2008. A structural glaciological analysis of the 2002 Larsen B ice shelf collapse. J. Glaciol. 54 (184), 3–16.
Han, H., Lee, H., 2014. Tide deflection of Campbell Glacier Tongue, Antarctica, analyzed by double-differential SAR interferometry and finite element method. Remote Sens. Environ. 141, 201–213.
Han, H., Lee, H., 2015. Tide-corrected flow velocity and mass balance of Campbell Glacier Tongue, East Antarctica, derived from interferometric SAR. Remote Sens. Environ. 160, 180–192.
Haug, T., Kaab, A., Skvarca, P., 2010. Monitoring ice shelf velocities from repeat MODIS and Landsat data - a method study on the Larsen C ice shelf, Antarctic Peninsula, and 10 other ice shelves around Antarctica. Cryosphere 4, 161–178.
Heid, T., Kaab, A., 2012. Evaluation of existing image matching methods for deriving glacier surface displacements globally from optical satellite imagery. Remote Sens. Environ. 118, 339–355.
Jacobs, S.S., Jenkins, A., Giulivi, C.F., Dutrieux, P., 2011. Stronger ocean circulation and increased melting under Pine Island Glacier ice shelf. Nat. Geosci. 4, 519–523. http://dx.doi.org/10.1038/ngeo1188.
Jones, D.H., Gudmundsson, G.H., 2014. Tracking B-31 iceberg with two aircraft deployed sensors. Natural Hazards and Earth System Sciences Discussions. vol. 2, pp. 4609–4627.
Joughin, I., 2002. Ice-sheet velocity mapping: a combined interferometric and speckle-tracking approach. Ann. Glaciol. 34, 195–201.
Joughin, I., MacAyeal, D.R., 2005. Calving of large tabular icebergs from ice shelf rift systems. Geophys. Res. Lett. 32, L02501. http://dx.doi.org/10.1029/2004GL0.20978.
Joughin, I., Smith, B.E., Holland, D.M., 2010. Sensitivity of 21st century sea level to ocean-induced thinning of Pine Island Glacier, Antarctica. Geophys. Res. Lett. 37, L20502. http://dx.doi.org/10.1029/2010GL044819.
Kääb, A., 2005. Combination of SRTM3 and repeat ASTER data for deriving alpine glacier flow velocities in the Bhutan Himalaya. Remote Sens. Environ. 94, 463–474.
Kaab, A., Lefauconnier, B., Melvold, K., 2005. Flow field of Kronebreen, Svalbard, using repeated Landsat 7 and ASTER data. Ann. Glaciol. 42, 7–13.
Khazendar, A., Rignot, E., Larour, E., 2011. Acceleration and spatial rheology of Larsen C Ice Shelf, Antarctic Peninsula. Geophys. Res. Lett. 38, L09502. http://dx.doi.org/10.1029/2011GL046775.
Kim, J.-W., Kim, D.-J., Kim, S.H., Ha, H.K., Lee, S.H., 2015a. Disintegration and acceleration of Thwaites Ice Shelf on the Amundsen Sea revealed from remote sensing measurements. GISci. Remote Sens. 52 (4), 498–509.
Kim, M., Im, J., Han, H., Kim, J., Lee, S., Shin, M., Kim, H., 2015b. Landfast sea ice monitoring using multisensory fusion in the Antarctic. GISci. Remote Sens. 52 (2), 239–256.
Kwok, R., Curlander, J.C., McConnell, R., Pang, S.S., 1990. An ice-motion tracking system at the Alaska SAR Facility. IEEE J. Ocean. Eng. 15 (1), 44–54.
Lee, D.S., Storey, J.C., Choate, M.J., Hayes, R.W., 2004. Four years of Landsat-7 on-orbit geometric calibration and performance. IEEE Trans. Geosci. Remote Sens. 42 (12), 2786–2795.
Lenaerts, J.T.M., van den Broeke, M.R., van de Berg, W.J., van Meijgaard, E., Munneke, P.K., 2012. A new, high-resolution surface mass balance map of Antarctica (1979–2010) based on regional atmospheric climate modeling. Geophys. Res. Lett. 39, L04501. http://dx.doi.org/10.1029/2011GL050713.
MacGregor, J.A., Catania, G.A., Markowski, M.S., Andrews, A.G., 2012. Widespread rifting and retreat of ice-shelf margins in the eastern Amundsen Sea Embayment between 1972 and 2011. J. Glaciol. 58 (209), 458–466.
Mankoff, K.D., Jacobs, S.S., Tulaczyk, S.M., Stammerjohn, S.E., 2012. The role of Pine Island Glacier ice shelf basal channels in deep-water upwelling, polynyas and ocean circulation in Pine Island Bay, Antarctica. Ann. Glaciol. 53, 123–128.
Mouginot, J., Rignot, E., Scheuchl, B., 2014. Sustained increase in ice discharge from the Amundsen Sea Embayment, West Antarctica, from 1973 to 2013. Geophys. Res. Lett. 41, 1576–1584. http://dx.doi.org/10.1002/2013GL059069.
Noh, M.-J., Howat, I.M., 2015. Automated stereo-photogrammetric DEM generation at high latitudes: surface extraction with TIN-based search-space minimization (SETSM) validation and demonstration over glaciated regions. GISci. Remote Sens. 52 (2), 198–217.
Pritchard, H.D., Ligtenberg, S.R., Fricker, H.A., Vaughan, D.G., van den Broeke, M.R., Padman, L., 2012. Antarctic ice-sheet loss driven by basal melting of ice shelves. Nature 484, 502–505. http://dx.doi.org/10.1038/nature10968.
Racoviteanu, A.E., Williams, M.W., Barry, R.G., 2008. Optical remote sensing of glacier characteristics: a review with focus on the Himalaya. Sensors 8, 3355–3383.
Rignot, E., 2002. Ice-shelf changes in Pine Island Bay, Antarctica, 1947–2000. J. Glaciol. 48 (161), 247–256.
Rignot, E., Vaughan, D.G., Schmeltz, M., Dupont, T., MacAyeal, D., 2002. Acceleration of Pine Island and Thwaites Glaciers, West Antarctica. Ann. Glaciol. 34, 189–194.
Rignot, E., Thomas, R.H., Kanagaratnam, P., Casassa, G., Frederick, E., Gogineni, S., Krabill, W., Rivera, A., Russell, R., Sonntag, J., Swift, R., Yungel, J., 2004. Improved estimation of the mass balance of glaciers draining into the Amundsen Sea sector of West Antarctica from the CECS/NASA 2002 campaign. Ann. Glaciol. 39, 231–237.
Rignot, E., Mouginot, J., Scheuchl, B., 2011a. Ice flow of the Antarctic ice sheet. Science 333 (6048), 1427–1430. http://dx.doi.org/10.1126/science.1208336.

Rignot, E., Mouginot, J., Scheuchl, B., 2011b. Antarctic grounding line mapping from differential satellite radar interferometry. Geophys. Res. Lett. 38, L10504. http://dx.doi.org/10.1029/2011GL047109.
Rignot, E., Jacobs, S., Mouginot, J., Scheuchl, B., 2013. Ice-shelf melting around Antarctica. Science 341 (6143), 266–270. http://dx.doi.org/10.1126/science.1235798.
Rignot, E., Mouginot, J., Morlighem, M., Seroussi, H., Scheuchl, B., 2014. Widespread, rapid grounding line retreat of Pine Island, Thwaites, Smith, and Kohler glaciers, West Antarctica, from 1992 to 2011. Geophys. Res. Lett. 41, 3502–3509. http://dx.doi.org/10.1002/2014GL060140.
Robertson, R., 2013. Tidally induced increases in melting of Amundsen Sea ice shelves. J. Geophys. Res. Oceans 118, 3138–3145. http://dx.doi.org/10.1002/jgrc.20236.
Scambos, T.A., Dutkiewicz, M.J., Wilson, J.C., Bindschadler, R.A., 1992. Application of image cross-correlation to the measurement of glacier velocity using satellite image data. Remote Sens. Environ. 42, 177–186.
Scambos, T.A., Bohlander, J.A., Shuman, C.A., Skvarca, P., 2004. Glacier acceleration and thinning after ice shelf collapse in the Larsen B embayment, Antarctica. Geophys. Res. Lett. 31, L18402. http://dx.doi.org/10.1029/2004GL020670.
Scherler, D., Leprince, S., Strecker, M., 2008. Glacier-surface velocities in alpine terrain from optical satellite imagery—accuracy improvement and quality assessment. Remote Sens. Environ. 112, 3806–3819.
Scheuchl, B., Mouginot, J., Rignot, E., 2012. Ice velocity changes in the Ross and Ronne sectors observed using satellite radar data from 1997 and 2009. Cryosphere 6, 1019–1030.
Shepherd, A., Wingham, D.J., Mansley, J.A., Corr, H.F., 2001. Inland thinning of Pine Island Glacier, West Antarctica. Science 291 (5505), 862–864. http://dx.doi.org/10.1126/science.291.5505.862.
Skvarca, P., Raup, B., De Angelis, H., 2003. Recent behaviour of Glaciar Upsala, a fast-flowing calving glacier in Lago Argentino, southern Patagonia. Ann. Glaciol. 36, 184–188.
Stearns, L., Hamilton, G., 2005. A new velocity map for Byrd Glacier, East Antarctica, from sequential ASTER satellite imagery. Ann. Glaciol. 41, 71–76.
Storey, J., Choate, M., Lee, K., 2014. Landsat 8 Operational Land Imager on-orbit geometric calibration and performance. Remote Sens. 6 (11), 11127–11152.
Strozzi, T., Luckman, A., Murray, T., Wegmuller, U., Werner, C.L., 2002. Glacier motion estimation using SAR offset-tracking procedures. IEEE Trans. Geosci. Remote Sens. 40 (11), 2384–2391.
Vaughan, D.G., Corr, H.F.J., Ferraccioli, F., Frearson, N., O'Hare, A., Mach, D., Holt, J.W., Blankenship, D.D., Morse, D.L., Young, D.A., 2006. New boundary conditions for the West Antarctic ice sheet: Subglacial topography beneath Pine Island Glacier. Geophys. Res. Lett. 33, L09501. http://dx.doi.org/10.1029/2005GL025588.
Warner, R.C., Roberts, J.L., 2013. Pine Island Glacier (Antarctica) velocities from Landsat7 images between 2001 and 2011: FFT-based image correlation for images with data gaps. J. Glaciol. 59 (215), 571–582.
Wen, J.H., Wang, Y.F., Wang, W.L., Jezek, K.C., Liu, H.X., Allison, I., 2010. Basal melting and freezing under the Amery Ice Shelf, East Antarctica. J. Glaciol. 56 (195), 81–90.
Young, N.W., Hyland, G., 2002. Velocity and strain rates derived from InSAR analysis over the Amery Ice Shelf, East Antarctica. Ann. Glaciol. 34, 228–234.